A Power Management Scheme for Grid-connected PV Integrated with Hybrid Energy Storage System

Anindya Bharatee, *Student Member*, *IEEE*, Pravat K. Ray, *Senior Member*, *IEEE*, and Arnab Ghosh, *Senior Member*, *IEEE*

***Abstract*—The penetration of renewable energy sources (RESs) in the distribution system becomes a challenge for the reliable and safe operation of the existing power system. The sporadic characteristics of sustainable energy sources along with the random load variations greatly affect the power quality and stability of the system. Hence, it requires storage systems with both high energy and high power handling capacity to coexist in microgrids. An efficient energy management structure is designed in this paper for a grid-connected PV system combined with hybrid storage of supercapacitor and battery. The combined supercapacitor and battery storage system grips the average and transient power changes, which provides a quick control for the DC-link voltage, i.e., it stabilizes the system and helps achieve the PV power smoothing. The average power distribution between the power grid and battery is done by checking the state of charge (SOC) of a battery, and an effective and efficient energy management scheme is proposed. Additionally, the use of a supercapacitor lessens the current stress on the battery system during unexpected disparity in the generated power and load requirement. The performance and efficacy of the proposed energy management scheme are justified by simulation studies.**

***Index Terms*—Hybrid microgrid, power management, hybrid energy storage arrangement, supercapacitor, battery.**

I. Introduction

TODAY'S power system emphasizes the growing adoption of green technologies due to the concern on energy saving and the fast penetration of renewable sources. The most commonly used environmental technologies nowadays are wind turbines and photovoltaic (PV). In terms of reliability and sustainability, the best choice is PV due to the advantages like low cost, high efficiency, low maintenance, and high consistency. However, due to the changing environmental operating conditions such as temperature, irradiance, effects of partial shading, and humidity, the stability and generation of the PV are affected up to a large extent, which adversely affects the stability of the connected system [1]. Energy storage systems (ESSs) are employed in the microgrids to provide continuous power from an intermittent source like PV, decrease the power mismatch between the generated and required power, i.e., the smoothing output power mode, and enhance the quality and stability of the system. The most popular and basic energy storage used is the battery because of its easy implementation. However, batteries have high energy density and small power density, which provide low charging/discharging rates. The supercapacitors possess a small energy density and high power density in contrast to the batteries, which give high charging/discharging rates. Hence, hybrid energy storage systems (HESSs) are created by grouping the battery and supercapacitor to get the benefits of both devices. In HESS, the life span of the batteries increases by distracting the battery momentary current to the supercapacitors [2].

A strategy for proper power supervision is essential for the effective and smooth operation of the hybrid microgrid. The strategy should provide services like ① regulating the terminal power of each distributed generator (DG), ② controlling the frequency and voltage of the system, ③ keeping the power balance among generation and demand, ④ supplying cost-effective power, ⑤ regulating DC-link voltage, ⑥ enhancing power qualities, ⑦ transitioning the smooth and seamless operating mode, and ⑧ maintaining the state of charge (SOC) of energy storage devices within their limits [3].

Different power management approaches for hybrid microgrid have been discussed in various researches. A unified control and power management scheme (CAPMS) is presented in [4] which utilizes a centralized control technique for effective and smooth control of power transfer among the utility grid, loads, and generating sources. The CAPMS is implemented in a PV-battery system in both isolated and grid-interactive modes. The power quality issues are not taken into consideration. In [5], a centralized optimization problem is developed in advance for effective power management and voltage control in the system. One diesel generator is used as a backup under extreme conditions of renewable sources and storage devices. The issues like frequent switching, delay in starting, and uneven loading in diesel generators are managed properly for smooth flow of power. A sliding mode control (SMC) based proportional-integer (PI) controller design is proposed in [6] for the DC-bus voltage regulation

Manuscript received: January 12, 2021; revised: March 13, 2021; accepted: June 29, 2021. Date of CrossCheck: June 29, 2021. Date of online publication: September 17, 2021.

A. Bharatee, P. K. Ray (corresponding author), and A. Ghosh are with the Department of Electrical Engineering, National Institute of Technology, Rourkela, 769008, India (e-mail: bharatee. anindya@gmail. com; rayp@nitrkl. ac. in; ghosha@nitrkl.ac.in).

DOI: 10.35833/MPCE.2021.000023

and dynamic sharing of power in hybrid energy storage based DC microgrid. This method effectively reduces the stress from the battery by diverting the uncompensated battery current to the supercapacitor unit. Reference [7] suggests an energy management structure for both grid-interactive and islanded modes of operation with HESS having a battery and supercapacitor. The features like reduction in current harmonics, improvement in power factor, and reactive power support are also realized from this scheme. In [8], a coordinated control approach for PV-wind-battery-connected hybrid system is suggested. A model predictive control scheme for both isolated and grid-connected modes is used for voltage source converter (VSC) control to keep the bus voltage stable and to enable smooth grid synchronization. A power management method based on multi-segment adaptive droop control is proposed in [9] for a PV and battery-connected islanded system. This method can track and provide the maximum PV power to the system as per the requirement and it can also change its operating point. A peak power management method is suggested in [10], which aims to reduce the burden during peak deficit power from the conventional power grid and to maximize the utilization of renewable energies. The suggested management scheme is developed by considering the peak demand, total demand, total generation, and the SOC of storage arrangements. A power management structure based on adaptive droop control is designed in [11]. In general, the adaptive droop control is designed for the optimum charging and discharging control of battery storages to ensure the longevity of the system with variation in power generation. In [12], control and power management techniques are discussed to track the operating point of the power converters at a faster rate for a better dynamic response along with the reduction of charging/discharging rate of the battery.

Considering the above surveys, an energy management structure is recommended in this paper for a grid-interactive PV with battery and supercapacitor unit. The key benefits found from the proposed scheme are: ① fast restoration of the DC bus voltage under variable generation and load power; ② the maintaining of voltage and frequency within the permissible limits according to IEEE standard 929-2000 [13]; ③ the lessening of the current stress from the battery; ④ the enhancement of power quality; and ⑤ rigorous computations are not required.

This rest of this paper is arranged as follows. Section II briefly explains the system architecture and power management scheme. The control structures for converters are described in Section III. The simulation results and discussion are presented in Section IV. Finally, Section V provides the conclusion.

II. System Architecture and Power Management Scheme

The architecture of grid-coupled PV with HESS is presented in Fig. 1, where L_1, L_2, C_1, and C_2 are the inductors and capacitors connected to quadratic boost converter, respectively; D_1, D_2, and D_3 are the diodes of quadratic boost converter; V_g, V_{dc}, and V_B are the grid voltage, voltage at DC bus, and battery voltage, respectively; C_b and C_{db} are the capacitors of the battery and bi-directional converter, respectively; C_{sc} is the supercapacitor capacitance; L_f, R_f, and C_f are the inductance, resistance, and capacitance of the LC filter, respectively; V_{sc} is the terminal voltage of supercapacitor; V_{pv} is the open-circuit voltage of PV; S is the switch of quadratic boost converter; S_1, S_2, S_3, and S_4 are the insulated gate bipolar transistor (IGBT) switches of the microgrid converter; S_{b1} and S_{b2} are the IGBT switches of the battery bi-directional converter; R_{nl} and L_{nl} are the resistor and inductor connected to 1φ bridge rectifier for non-linear load, respectively; R_{Lac} and R_{Ldc} are the resistive AC and DC linear loads, respectively; L_b is the inductor connected to battery bi-directional converter; R_b is the resistor connected to battery bi-directional converter; L_{sc} is the inductor connected to the supercapacitor bi-directional converter; and S_{S1} and S_{S2} are the IGBT switches of the supercapacitor bi-directional converter. To get the required DC-link voltage, the output voltage of DC-DC converter should be sufficiently high for the integration of a low-voltage PV system with the distribution system. Hence, a quadratic boost converter is used with a PV system to get a high conversion ratio with high efficiency for a wide range of voltage [14]. For energy storage, supercapacitors and batteries are utilized along with the bi-directional boost DC-DC converter (BDDC) for the regulation of power transfer among the grid and the ESSs. The AC utility grid is linked to the DC microgrid via a VSC, which can operate as an inverter or a rectifier according to the mode of operation. The LC filter is used at the output of VSC to smooth the voltages and currents at the AC side. In this system, both linear and non-linear loads are connected to check the performance of the proposed scheme under different operating conditions.

This power management structure mainly comprises the generation of reference current, an algorithm for power management, and control of various currents converters. The suggested power management arrangement for grid-connected system is explained in Fig. 2, where P_{Ravg} and P_{Rtrans} are the average and transient power required for PV, respectively; and i_{pvr} is the reference PV current. A low pass filter (LPF) is used to extract the average current component for the utility grid and battery [15], [16]. The transient current for the supercapacitor is extracted by taking away the average current from the total required current. Also, an error co-efficient of uncompensated battery current is added to the transient current to advance the dynamics of DC-link voltage. A moving average filter (MAF) is employed to estimate the AC load requirement. MAF is a linear phase finite impulse response (FIR) filter that can operate as an ideal LPF under some specific conditions [17]. Depending on the PV generation and load requirement, the power management algorithm (PMA) selects the mode of operation and produces the current references. Then, these reference currents undergo the current control stages and finally, produce the switching pulses for all the power converters.

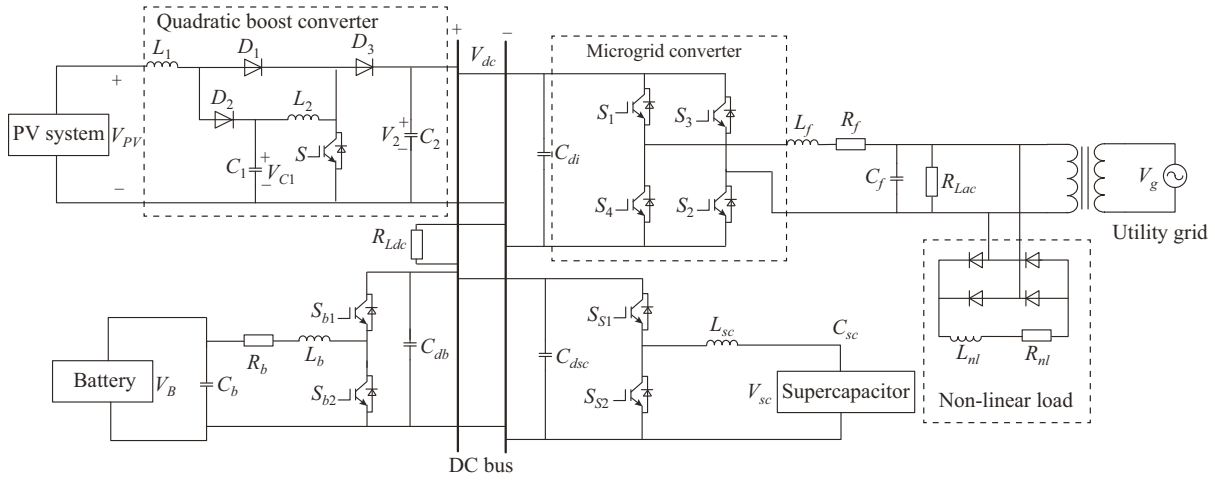

Fig. 1. Architecture of grid-coupled PV with HESS.

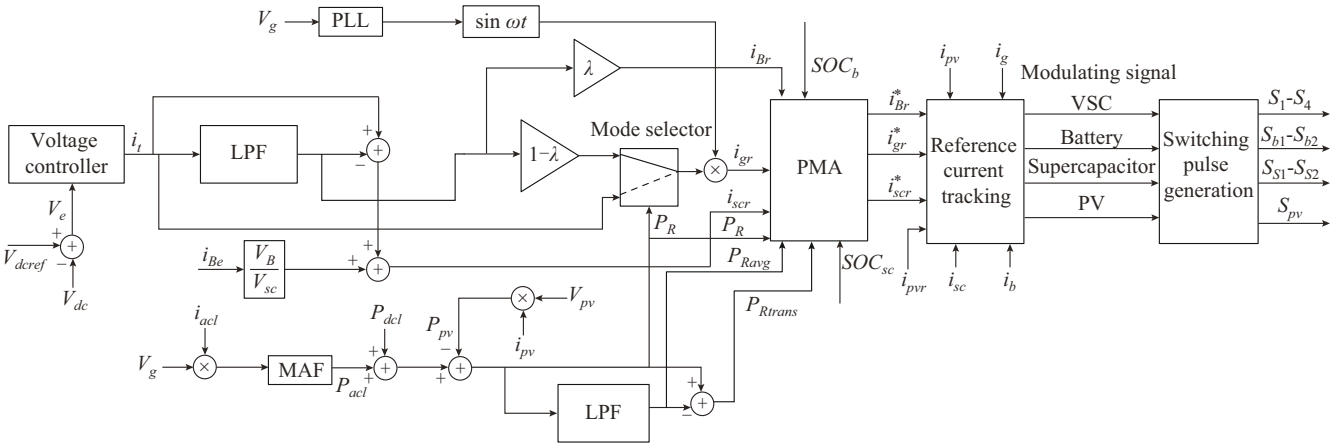

Fig. 2. Suggested power management arrangement for grid-connected system.

A. Reference Current Generation for Grid and HESS

In practical operation, a grid-coupled DC microgrid depends on the distribution of power among the PV, ESSs, and the AC utility grid. A complete power equilibrium should be kept to get a stable system. The power balance is:

$$P_g(t)+P_{pv}(t)+P_B(t)+P_{sc}(t)-P_l(t)=P_t(t) \tag{1}$$

where $P_g(t)$, $P_{pv}(t)$, $P_B(t)$, and $P_{sc}(t)$ are the corresponding power of the grid, renewable source, batteries, and supercapacitor unit, respectively; and $P_l(t)=P_{dcl}(t)+P_{acl}(t)$ is the sum of both DC and AC load power. V_{dc} is the reproduction of power equilibrium between the generations and demands [15]. The total power required at the DC-link for power balancing can be separated into two components: average power component $\bar{P}_t(t)$ and transient power component $P_t'(t)$. The total power and the respective current are:

$$P_t(t)=\bar{P}_t(t)+P_t'(t)=V_{dc}i_t(t) \tag{2}$$

$$i_t(t)=\frac{\bar{P}_t(t)}{V_{dc}}+\frac{P_t'(t)}{V_{dc}}=\bar{i}_t(t)+i_t'(t) \tag{3}$$

where $i_t(t)$ is the operative current; $\bar{i}_t(t)$ is the average value; and $i_t'(t)$ is the transient value of operative current. The operative current at the DC bus results from a voltage controller and is specified in (4).

$$i_t(t)=\bar{i}_t(t)+i_t'(t)=K_{pvd}V_e+K_{ivd}\int v_e\mathrm{d}t \tag{4}$$

where V_e, K_{pvd}, and K_{ivd} are the DC-link error voltage, proportional and integral coefficients of the voltage control loop, respectively.

An LPF is used to extract $\bar{i}_t$ from the total current and allotted to the PV, battery, and power grid [15]. The transient current is provided by the supercapacitor.

$$\bar{i}_t(s)=\frac{\omega_c}{s+\omega_c}i_t(s) \tag{5}$$

$$\begin{cases} i_{Br}(s)=\lambda\bar{i}_t(s) \\ i_{gr}(s)=(1-\lambda)\bar{i}_t(s) \end{cases} \tag{6}$$

$$i_t'(s)=\left(1-\frac{\omega_c}{s+\omega_c}\right)i_t(s) \tag{7}$$

where ω_c, $i_{Br}(s)$, $i_{gr}(s)$, and λ are the cut-off frequency of LPF, reference current for battery, reference current for grid, and power sharing coefficient, respectively. The cut-off frequency of LPF is set to be 6.283 rad/s. The main focus of the sharing coefficient is to decrease the rate of change of battery current throughout the normal working state and un-

expected power oscillations and to keep the SOC of the battery within the limit for a longer period [18]. The value of the sharing coefficient depends on the SOC of the battery SOC_b. The logic for λ in insufficient power mode (IPM) is shown in Table I [18], where U and L are the upper and lower limits of SOC, respectively.

TABLE I
LOGIC FOR λ IN IPM

$SOC_b(t)$	λ	$1-\lambda$
$0.7<SOC_b<U$	1.0	0
$0.5<SOC_b<0.7$	0.6	0.4
$0.1<SOC_b<0.5$	0.3	0.7
$SOC_b<L$	0	1.0

B. Proposed Method for Power Management

The PMA chooses the working condition of the system depending on the availability of the generated power and load power. By setting (8), three power modes P_R of operation are recognized as follows.

$$P_R = P_l - P_{pv} \tag{8}$$

1) IPM: $P_R > 0$.
2) Sufficient power mode (SPM): $P_R < 0$.
3) Floating power mode (FPM): $P_R = 0$.

Depending on the SOCs of battery and supercapacitor, each power mode is again classified as four operating ideas. The SOCs of battery and supercapacitor SOC_b and SOC_{sc} can be estimated by using the Coulomb counting method [9], [19], as shown in Fig. 3. In Fig. 3, i_b, i_{sc}, SOC_{b0}, SOC_{SC0}, and C_N are the battery current, supercapacitor current, initial SOC of battery, initial SOC of supercapacitor, and nominal capacity of battery [20], respectively.

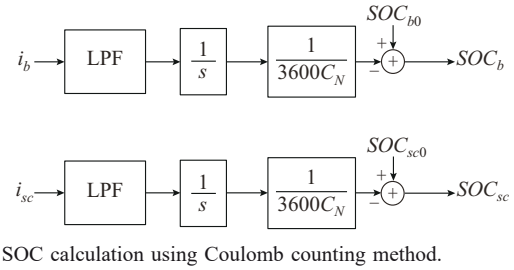

Fig. 3. SOC calculation using Coulomb counting method.

1) IPM

In this power mode, the required load is more than the PV generated power. Hence, the average deficit power demand is handled by the main grid, PV, and battery till the SOC of the battery is within the limits and the transient power component is handled by the supercapacitor until it reaches its lower SOC boundary. When the SOC of the supercapacitor is less than the lower edge, the transient power and oscillatory power are handled by the main grid. According to the SOC limit of battery and supercapacitor, functional designs in IPM are given in Table II, where the symbol * denotes the battery reference current generated from power management algorithm. The power management in IPM is given in Table III, where P_{loss} is the power losses in the system; i_{loss} is the current losses of the system; $\bar{P}_R$ is the total average power requirement in the system; and P'_R is the transient component of power.

TABLE II
FUNCTIONAL DESIGNS IN IPM

SOC limit	Reference current generation
$SOC_b>L$ and $SOC_{sc}>L$	$i^*_{Br}=\lambda\bar{i}_t,\ i^*_{scr}=i'_t,\ i^*_{gr}=(1-\lambda)\,\bar{i}_t$
$SOC_b<L$ and $SOC_{sc}>L$	$i^*_{Br}\cong 0,\ i^*_{scr}=i'_t,\ i^*_{gr}=\bar{i}_t$
$SOC_b>L$ and $SOC_{sc}<L$	$i^*_{Br}=\lambda\bar{i}_t,\ i^*_{scr}\cong 0,\ i^*_{gr}=(1-\lambda)\,\bar{i}_t+i'_t$
$SOC_b<L$ and $SOC_{sc}<L$	$i^*_{Br}\cong 0,\ i^*_{scr}\cong 0,\ i^*_{gr}=i_t$

TABLE III
POWER MANAGEMENT IN IPM

SOC limit	Reference power
$SOC_b>L$ and $SOC_{sc}>L$	$P^*_B(t)=\lambda\bar{P}_R,\ P^*_{sc}(t)=P'_R,\ P_g(t)=(1-\lambda)\,\bar{P}_R+P_{loss}$
$SOC_b<L$ and $SOC_{sc}>L$	$P^*_B(t)\cong 0,\ P^*_{sc}(t)=P'_R,\ P_g(t)=\bar{P}_R+P_{loss}$
$SOC_b>L$ and $SOC_{sc}<L$	$P^*_B(t)=\lambda\bar{P}_R,\ P^*_{sc}(t)\cong 0,\ P_g(t)=(1-\lambda)\,\bar{P}_R+P'_R+P_{loss}$
$SOC_b<L$ and $SOC_{sc}<L$	$P^*_B(t)\cong 0,\ P^*_{sc}(t)\cong 0,\ P_g(t)=P_R+P_{loss}$

2) SPM

In this power mode, the PV power production is more than the required load. The excess power is utilized for the battery and supercapacitor charging until they gain their upper SOC limits. When the battery and supercapacitor grasp their higher SOC limits, i. e., completely charged, then the surplus power is inserted into the main grid via VSC. The functional designs in SPM are defined in Table IV and the power management in SPM is given in Table V.

TABLE IV
FUNCTIONAL DESIGNS IN SPM

SOC limit	Reference current generation
$SOC_b<U$ and $SOC_{sc}<U$	$i^*_{Br}=i_{B,ch},\ i^*_{scr}=i_{sc,ch},\ i^*_{gr}=i_t$
$SOC_b<U$ and $SOC_{sc}>U$	$i^*_{Br}=i_{B,ch},\ i^*_{scr}=i'_t,\ i^*_{gr}=i_t-i_{scr}$
$SOC_b>U$ and $SOC_{sc}<U$	$i^*_{Br}\cong 0,\ i^*_{scr}=i_{sc,ch},\ i^*_{gr}=i_t$
$SOC_b>U$ and $SOC_{sc}>U$	$i^*_{Br}\cong 0,\ i^*_{scr}=i'_t,\ i^*_{gr}=i_t-i_{scr}$

TABLE V
POWER MANAGEMENT IN SPM

SOC limit	Reference power
$SOC_b<U$ and $SOC_{sc}<U$	$P^*_B(t)=-P_{Br},\ P^*_{sc}(t)=-P_{scr},\ P_g(t)=P_{loss}$
$SOC_b<U$ and $SOC_{sc}>U$	$P^*_B(t)=-P_{Br},\ P^*_{sc}(t)\cong 0,\ P_g(t)=P_{loss}$
$SOC_b>U$ and $SOC_{sc}<U$	$P^*_B(t)\cong 0,\ P^*_{sc}(t)=-P_{scr},\ P_g(t)=P_{loss}$
$SOC_b>U$ and $SOC_{sc}>U$	$P^*_B(t)\cong 0,\ P^*_{sc}(t)\cong 0,\ P_g(t)=P_{loss}-P_R$

3) FPM

In this power mode, the PV power generation is more or less than the load requirement. In this situation, the utility grid provides the power to charge the battery and supercapacitor till they gain their higher SOC boundaries. When the storage devices are completely charged, the battery becomes

idle and the supercapacitor continues to supply the transient power. The functional designs in FPM are given in Table VI and the power management in FPM is given in Table VII. Here, $i_{B,ch}=-P_{Br}/V_B$ is the rated charging current for battery; $i_{sc,ch}=-P_{scr}\sqrt{C_{sc}/(2E_{scr})}$ is the rated charging current for supercapacitor; P_{Br} and P_{scr} are the rated battery and supercapacitor power, respectively; and E_{scr} is the energy stored in supercapacitor.

TABLE VI
FUNCTIONAL DESIGNS IN FPM

SOC limit	Reference current generation
$SOC_b<U$ and $SOC_{sc}<U$	$i_{Br}^*=i_{B,ch}$, $i_{scr}^*=i_{sc,ch}$, $i_{gr}^*=i_{Br}^*+i_{scr}^*$
$SOC_b<U$ and $SOC_{sc}>U$	$i_{Br}^*=i_{B,ch}$, $i_{scr}^*=i_t'$, $i_{gr}^*=i_{Br}^*$
$SOC_b>U$ and $SOC_{sc}<U$	$i_{Br}^*\cong 0$, $i_{scr}^*=i_{sc,ch}$, $i_{gr}^*=i_{scr}^*$
$SOC_b>U$ and $SOC_{sc}>U$	$i_{Br}^*\cong 0$, $i_{scr}^*=i_t'$, $i_{gr}^*=i_{loss}$

TABLE VII
POWER MANAGEMENT IN FPM

SOC limit	Reference power
$SOC_b<U$ and $SOC_{sc}<U$	$P_B^*(t)=-P_{Br}$, $P_{sc}^*(t)=-P_{scr}$, $P_g(t)=P_{Br}+P_{scr}+P_{loss}$
$SOC_b<U$ and $SOC_{sc}>U$	$P_B^*(t)=-P_{Br}$, $P_{sc}^*(t)=P_R'$, $P_g(t)=P_{Br}+P_{loss}$
$SOC_b>U$ and $SOC_{sc}<U$	$P_B^*(t)\cong 0$, $P_{sc}^*(t)=-P_{scr}$, $P_g(t)=P_{scr}+P_{loss}$
$SOC_b>U$ and $SOC_{sc}>U$	$P_B^*(t)\cong 0$, $P_{sc}^*(t)=P_R'$, $P_g(t)=P_{loss}$

III. CONTROL STRUCTURE FOR CONVERTERS

A. Modeling of Converter Control for HESS

The converter control comprises the production of reference current i_{Br}^*, PMA, and the selection of the average power sharing constant λ depending on battery SOC in the IPM, as shown in Fig. 4. In Fig. 4, PWM stands for pulse width modulation. For the bi-directional converter connected to the battery, the reference current $i_{Br}^*(t)$ and modulating signal δ_B are defined as:

$$i_{Br}^*(t)=f_{B,PMA}\lambda\frac{1}{T_B}\int_{t_0-T_B}^{t_0}i_t(t)\,\mathrm{d}t \tag{9}$$

$$\delta_B=K_{pB}i_{Be}(t)+\frac{K_{iB}}{T_B}\int_{t-T_B}^{t}i_{Be}(t)\,\mathrm{d}t \tag{10}$$

where t_0, $f_{B,PMA}$, and T_B are the arbitrary time instant, objectives for battery control specified in PMA, and battery average block window length, respectively; and i_{Be}, K_{pB}, and K_{iB} are the error current of battery, proportional and integral coefficients of battery PI controller, respectively.

The control structure for supercapacitor mostly involves the generation of reference current, an algorithm for power management, and control of BDDC, as shown in Fig. 4. The supercapacitor handles the high frequency momentary component of the total operative current at the DC link by using an LPF, which is given by:

$$i_{scr}(s)=i_t(s)-\frac{\omega_c}{s+\omega_c}i_t(s)+G'i_{Be}(s) \tag{11}$$

wher G' is the factor for compensation of battery error current.

The computed reference current by using (11) is provided to the PMA. By considering the other input variable quantities like SOC_b, SOC_{sc}, and P_R, PMA chooses the working mode for the supercapacitor. Then, the reference current generated by the PMA is passed through the current regulator to yield the switching pulses for the supercapacitor converter. The current reference and the controlling signal for the supercapacitor converter are calculated by:

$$i_{scr}^*(t)=f_{sc,PMA}i_{scr}(t) \tag{12}$$

$$\delta_{sc}=K_{psc}i_{sce}(t)+\frac{K_{isc}}{T_{sc}}\int_{t-T_{sc}}^{t}i_{sce}(t)\,\mathrm{d}t \tag{13}$$

where $f_{sc,PMA}$, i_{sce}, T_{sc}, K_{psc}, and K_{isc} are the PMA defined objectives for supercapacitor, error in supercapacitor current, average block window length of supercapacitor, proportional and integral constants of PI controller, respectively.

$$G'=\frac{V_B}{V_{sc}} \tag{14}$$

The alteration of uncompensated battery current to supercapacitor system provides faster DC-link voltage restoration.

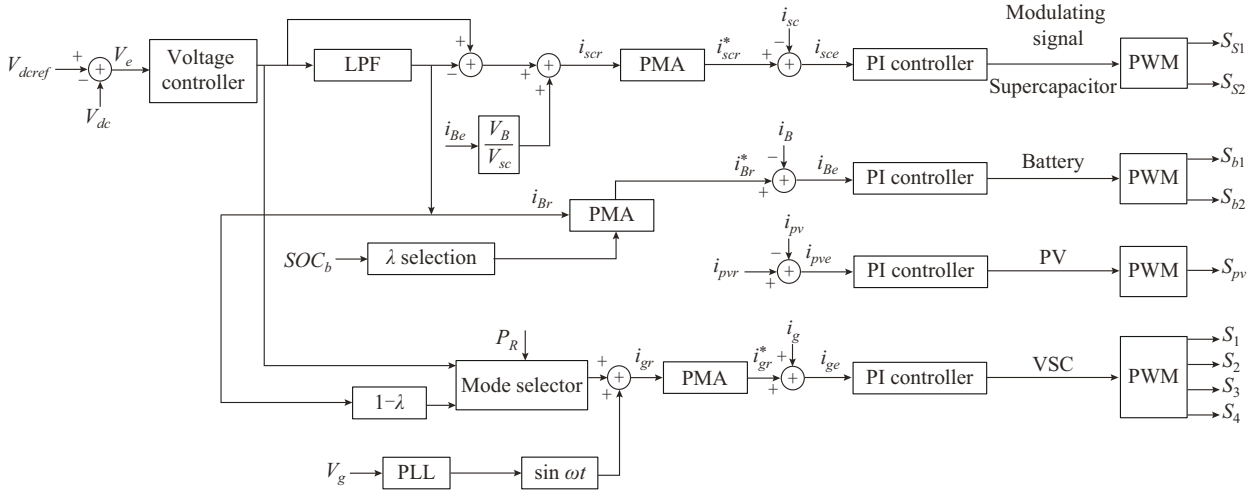

Fig. 4. Converter control for supercapacitor, battery, PV, and utility grid.

B. Modeling of Control for PV Converter

The reference current of PV converter should be chosen such that the arrangement could function in all three probable approaches explained in Section II. The preferred PV reference current i_{pvr} and the genuine current of the high gain PV converter is then compared and controlled using a PI regulator as shown in Fig. 4. The PV converter controlling signal δ_{pv} is stated as:

$$\delta_{pv} = K_{ppv} i_{pv}(t) + \frac{K_{ipv}}{T_{pv}} \int_{t-T_{pv}}^{t} i_{pve}(t)\, \mathrm{d}t \tag{15}$$

where i_{pve}, T_{pv}, K_{ppv}, and K_{ipv} are the error current of PV, PV average block window length, proportional and integral coefficients of PI controller, respectively.

C. Control Structure for VSC

The generation of reference current, voltage template computation using a phase-locked loop (PLL), and current controller are the key parts of VSC as shown in Fig. 4. Depending on the availability of the generated power and load power, the VSC can act as an inverter or a converter. Hence, the VSC current reference is produced by considering the bi-directional power flow. The VSC reference current is given as:

$$i_{gr} = \begin{cases} (1-\lambda)\bar{i}_t(t)\sin\omega t & P_R > 0 \ \ (\text{insufficient}) \\ \bar{i}_t \sin\omega t & P_R < 0 \ \ (\text{sufficient}) \end{cases} \tag{16}$$

where ω is the grid angular frequency.

IV. Simulation Results and Discussion

To validate the proposed scheme, simulations are conducted in the MATLAB 9.6.1.1072779 (R2019a) software environment.

A. Parameter Assessment of Proposed Scheme

The choice of several components in the proposed scheme, e. g., DC-bus voltage, DC-link capacitor, ripple filter, cut-off frequency for MAF, IGBTs, depends on the design provisions. The minimum value of DC-bus voltage should be chosen as twice of the peak of phase voltage [16]. The value of DC- link capacitor can be obtained by using (17).

$$C_{di} = \frac{3V\alpha It}{\frac{1}{2}\left(V_{dc}^2 - V_{dc,\min}^2\right)} \tag{17}$$

where V is the phase voltage; α is overload factor; I is the phase current; t is the time by which DC bus voltage should be retrieved after any variation in power; V_{dc} is the DC-bus reference voltage; and $V_{dc,\min}$ is the minimum allowable DC-link voltage [16].

L_f can be estimated by using (18).

$$L_f = \frac{\sqrt{3}\, mV_{dc}}{12\alpha f_{sw}\Delta i} \tag{18}$$

where m, f_{sw}, and Δi are the modulation index, switching frequency of VSC, and current ripple in VSC, respectively [16]. Here, the overloading factor is 1.2 and the switching frequency is 20 kHz.

In practical power system, the non-triplen odd harmonic and odd harmonics are observed to be the most dominant harmonic components. To remove these harmonic components from the system, the window length of MAF should be half of the fundamental period of the grid voltage [17]. Hence, the cut-off frequency of MAF is taken as 100 Hz as the fundamental frequency of the system is 50 Hz.

The values of linear and non-linear loads are varied intentionally to justify the described conditions in the simulation. Also, the PV power generation is varied by changing the irradiance value for inspecting the validation of the proposed scheme with variation in generated power. The estimated system parameters and some other parameters from [18] are stated in Table VIII, where i_p is the maximum peak current and i_{mc} is the maximum continuous current.

TABLE VIII
Parameters Used For System Simulation

Specification	Parameter	Value
PV array	V_{pv}	40 V
	i_{pv}	20 A
Supercapacitor	V_{sc}	16.2 V
	i_p	200 A
	C_{sc}	58 F
	i_{mc}	19 A
Battery	C_B	14 Ah
	V_B	12 V
Battery BDDC	R_b	0.5 Ω
	L_b	5 mH
	C_b	220 μF
	C_{db}	220 μF
Supercapacitor BDDC	L_{sc}	5 mH
	C_{dsc}	220 μF
VSC	L_f	10 mH
	C_f	1 μF
	C_{di}	2200 μF
Quadratic boost PV converter	$L_1 = L_2$	5 mH
	C_1	110 μF
	C_2	220 μF
Linear and non-linear load parameters	R_{Ldc}	50 Ω
	R_{Lac}	10 Ω
	R_{nl}	30 Ω
	L_{nl}	1 mH
Utility grid	V_g	230 V
	f	50 Hz
DC bus voltage	V_{dc}	100 V
LPF	f_{LPF}	1 Hz
MAF	f_{MAF}	100 Hz

B. Performance with Variation in PV Power

The active performance of the planned control strategies under the condition of variation of PV power generation is shown in Figs. 5 and 6. The PV power generation is varied at $t = 2$ s by changing the irradiance of the system from 1000 W/m^2 to 600 W/m^2. The reduction in PV power generation at 2 s is noticeable in Fig. 6. Irrespective of the change in PV power, the DC bus voltage regains its constant value within 0.15 s with an undershoot 1 V, which is within the permissible limit as per IEEE standard of 929-2000 [13] as

shown in Fig. 5. At the point of change, the transient power surge is handled by the supercapacitor unit. The average component is compensated by the battery units and grid combinedly and preserves the constant DC link voltage. The combination of battery with supercapacitor effectively reduces the settling time and voltage dip at the point of PV generation change. As the settling time is reduced, the vicinity of the final value of the DC-bus voltage is reached very quickly within the specified error. The corresponding DC link, battery, and supercapacitor voltages are shown in Fig. 5 and respective power is shown in Fig. 6.

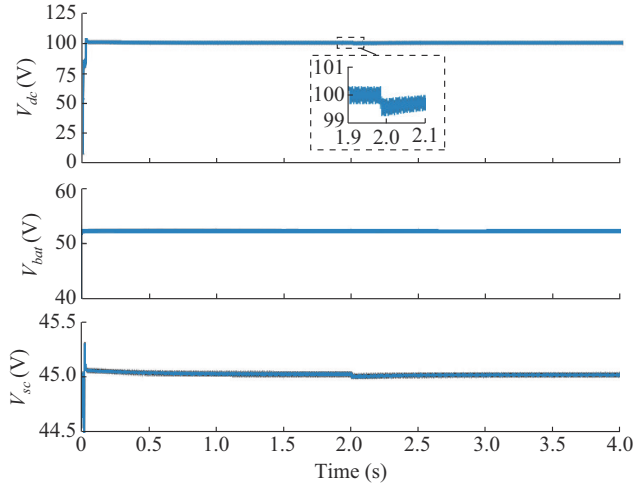

Fig. 5. Voltages of DC link, battery, and supercapacitor with PV power variation.

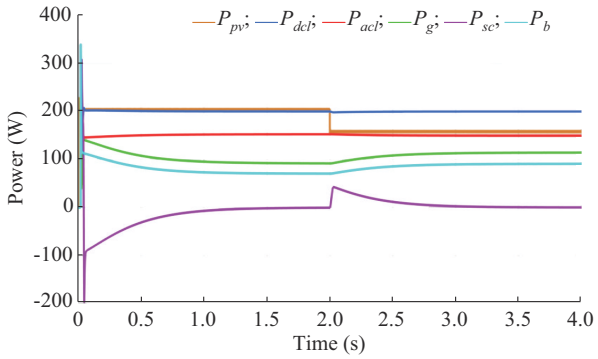

Fig. 6. Power of PV, DC load, AC load, utility grid, supercapacitor, and battery with PV power variation.

The total harmonic distortion (THD) of grid current with PV power variation is shown in Fig. 7. It is clearly observed from Fig. 7 that THD of utility grid current is 1.11%, which is within the acceptable THD range according to IEEE standard 519 [21]. As harmonics in the system can give rise to excessive heating in equipment, malfunction of electronics devices, and escalate the voltage stress and heating in capacitors, which can lead to the life reduction of appliances and more load losses in the system. Hence, the harmonics should be within the specified limits.

C. Performance with Variation in Load

The performance of the control strategies under the condition of load variation is shown in Figs. 8 and 9, and it is tested under insufficient power conditions. The DC load increases at $t=2$ s by varying the linear DC load from $R_{Ldc}=50\ \Omega$ to $R_{Ldc}=25\ \Omega$. The abrupt variation in DC load power at $t=2$ s is visible in Fig. 8. The average power demand to make the DC bus voltage persistent is handled by the power grid, and the batteries and the transient power are handled by the supercapacitor. Hence, irrespective of abrupt change in load requirements, the DC bus voltage undergoes a voltage dip of 2 V, which meets the acceptable limit [13], and regains its constant voltage within 0.2 s, as shown in Fig. 8.

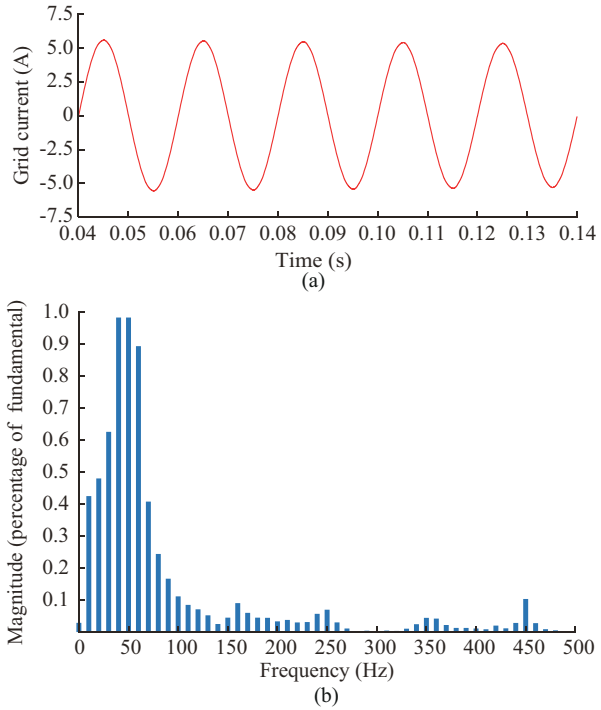

Fig. 7. THD of utility grid current with PV power variation.

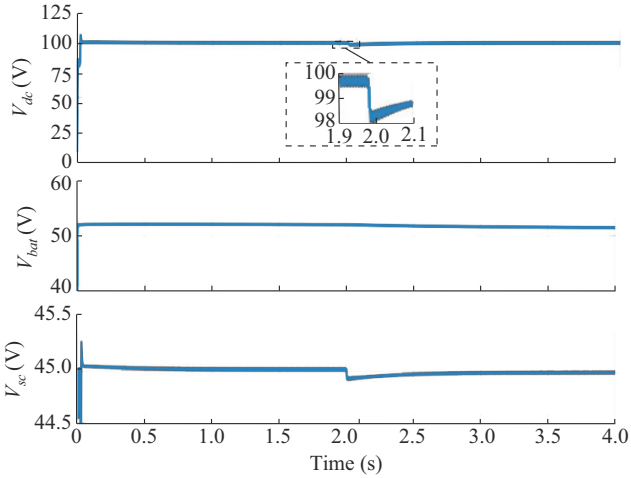

Fig. 8. Voltages of DC link, battery, and supercapacitor under load variation.

The frequency waveform with variation in load is shown in Fig. 10, where a frequency deviation of ±0.01 Hz is found at $t=2$ s when the load increases suddenly. The frequency deviation meets the standard allowable limit defined

in IEEE standard 929-2000 [13]. The frequency reference is extracted from the PLL and is assigned to VSC, which is responsible to retain the constant frequency of 50 Hz. When a microgrid is connected to any renewable source, the deviation in frequency significantly deteriorates the power quality provided to the loads. Hence, it is important to maintain the frequency within the limits for power quality enhancement.

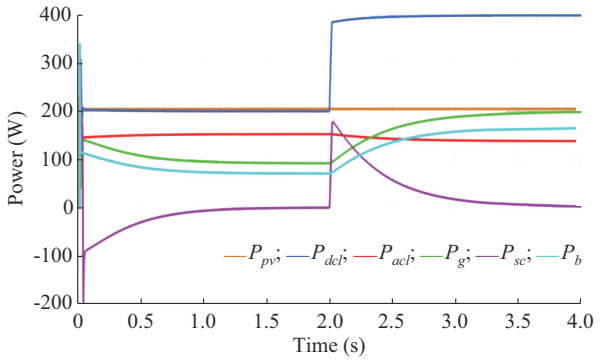

Fig. 9. Power of PV, DC load, AC load, utility grid, supercapacitor, and battery with variation in load.

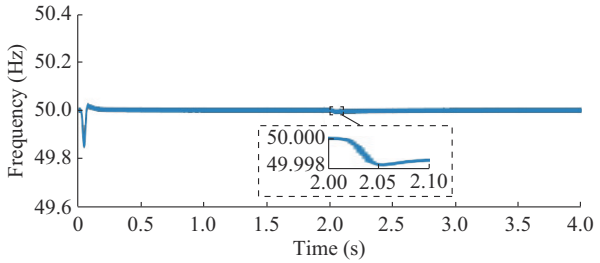

Fig. 10. Frequency waveform with variation in load.

D. Performance with IPM

By considering the SOC of the storage devices, four states are defined. In state 1, at t=0-2 s when $SOC_b > L$ and $SOC_{sc} > L$, the power grid and battery supply the average power requirement by using the concept of power sharing coefficient. The supercapacitor system deals with the rapidly varying transient power.

In state 2, at t=2-4 s when $SOC_b < L$ and $SOC_{sc} > L$, the total average power is handled by the power grid and the supercapacitor unit supplies the transient power. The battery becomes idle as the SOC of the battery goes down the lower boundary. The supercapacitor and the power grid combinedly make the DC link voltage constant.

In state 3, at t=4-6 s when $SOC_b > L$ and $SOC_{sc} < L$, the supercapacitor becomes idle and the total power is divided by the power grid and battery system until the SOC_b becomes less than lower boundary according to the concept of power sharing coefficient.

In state 4, at t=6-8 s when $SOC_b < L$ and $SOC_{sc} < L$, both battery and supercapacitor become idle. The total shortage of power demand is provided by the power grid only to make the DC link voltage constant. Irrespective of any state in IPM, the DC bus voltage restores very quickly as shown in Fig. 11. The SOCs of the storage devices are changed intentionally to validate the four substates. The respective changes in powers are shown in Fig. 12.

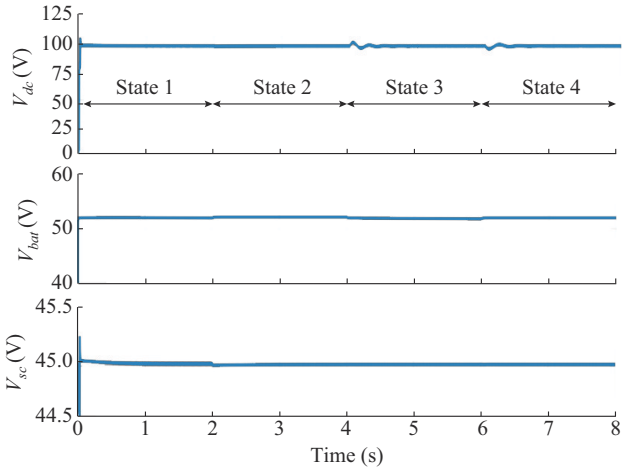

Fig. 11. Voltages of DC link, battery, and supercapacitor with IPM.

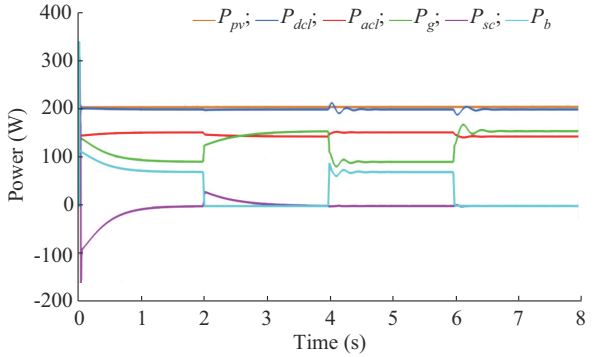

Fig. 12. Power of PV, DC load, AC load, utility grid, supercapacitor, and battery with IPM.

The VSC provides the harmonic components demanded by the non-linear loads connected to the system. Therefore, the grid current I_g attains the constancy and achieves the unity power factor at the grid side throughout the simulation as verified in Fig. 13.

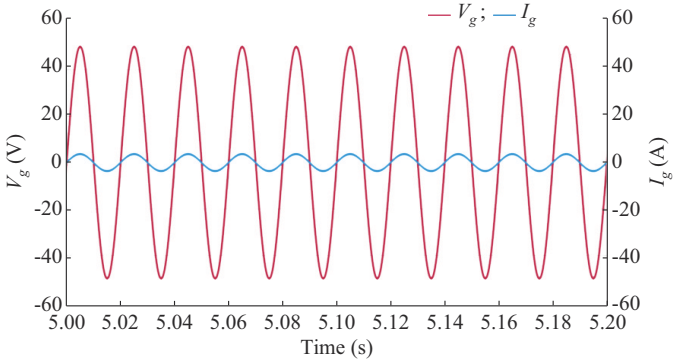

Fig. 13. Zoomed view of grid voltage and current with IPM.

In Fig. 14, the VSC current with IPM is shown. When the SOC_{sc} is within the defined limits, supercapacitor shares the transient requirement of the system, hence, a smooth change in VSC current is realized in Fig. 14 during states 1 and 2. However, when SOC_{sc} falls below the lower limit, it causes

a sudden change in VSC current as shown in Fig. 14. Hence, the supercapacitor plays an important role in the smooth operation of the microgrid.

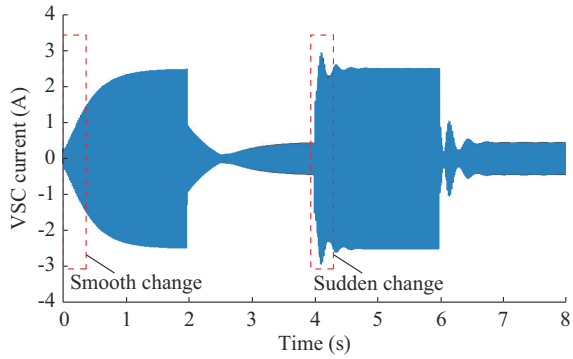

Fig. 14. VSC current with IPM.

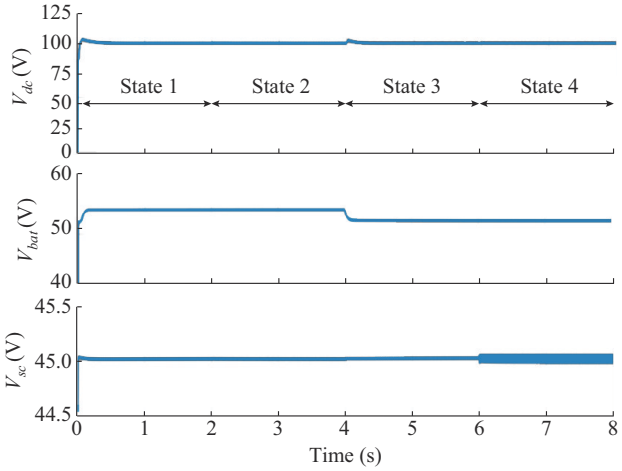

Fig. 15. Voltages of DC link, battery, and supercapacitor with SPM.

E. Performance with SPM

Four states are defined by considering the SOCs of the storage devices. In state 1, at t=0-2 s when $SOC_b < U$ and $SOC_{sc} < U$, the battery and the supercapacitor are charged based on their respective rated charging currents. After charging the storage devices, the remaining excess power is supplied to the power grid.

In state 2, at t=2-4 s when $SOC_b < U$ and $SOC_{sc} > U$, the battery is energized by its evaluated rated charging current until it grasps its upper SOC limit. The supercapacitor supplies the fast-changing transient power and the power grid handles the total average power.

In state 3, at t=4-6 s when $SOC_b > U$ and $SOC_{sc} < U$, the battery becomes idle and the supercapacitor is charged based on its rated charging current until it achieves its higher SOC limit. In this state, the grid handles the overall power demand of the system.

In state 4, at t=6-8 s when $SOC_b > U$ and $SOC_{sc} > U$, the battery becomes idle and the supercapacitor supplies the required transient power only. After supplying the loads, the excess power from the PV is supplied to the power grid. Irrespective of any state in SPM, the DC link voltage restores very quickly as shown in Fig. 15. The SOCs of the storage devices are changed intentionally to confirm the four described situations. The respective changes in power are shown in Fig. 16.

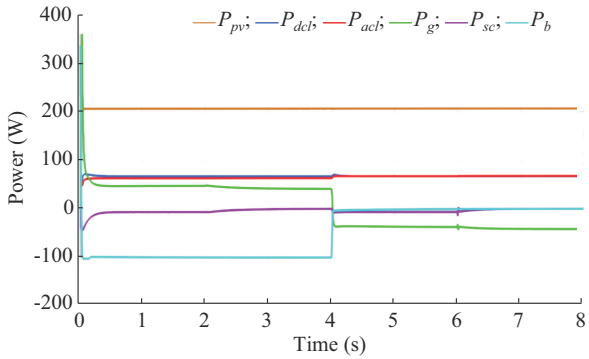

Fig. 16. Power of PV, DC load, AC load, utility grid, supercapacitor, and battery with SPM.

F. Performance Analysis of Various Power Management Schemes

To exhibit the robustness and effectiveness of the proposed scheme, the settling time t_s, voltage overshoot/undershoot M_p of DC-bus voltage, and the THD is analyzed for different schemes with variation in PV generation. The graphical comparison of different schemes is shown in Fig. 17, where scheme 1 is from [18], scheme 2 is from [22], and scheme 3 is from [12]. It is observed from the Fig. 17 that the proposed scheme is better compared with the other schemes as it has very little peak overshoot and settles down within a very small period with a less current harmonic in the power system.

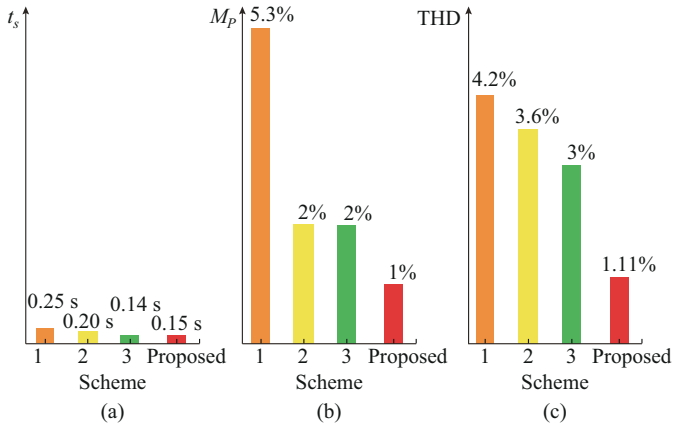

Fig. 17. Performance analysis of various power management schemes. (a) Settling time. (b) Voltage overshoot or undershoot. (c) THD.

V. Conclusion

A new power management scheme is proposed for the control of grid-connected PV systems along with hybrid energy storage devices. This scheme ensures some power quality features due to the use of HESSs along with the main purpose of bi-directional power flow. The objectives of the proposed scheme, e. g., faster DC voltage regulation, voltage and frequency regulation, maintenance of power quality issues, and keeping the SOC of storage systems within their

limits, are justified through simulation results. The potency of the discussed control technique is conveyed by comparing the power quality features like settling time, overshoot/undershoot, and THD with other different schemes. The proposed scheme does not comprise the peak and off-peak hour demand, which can be further included for better power management. The proposed scheme is verified through simulation results for grid-connected application. Hence, it can be applied for isolated microgrid system. Small signal analysis can be done subsequently to look over the system stability.

REFERENCES

[1] S. K. Kollimalla and M. K. Mishra, "A novel adaptive P&O MPPT algorithm considering sudden changes in the irradiance," *IEEE Transactions on Energy Conversion*, vol. 29, no. 3, pp. 602-610, May 2014.

[2] S. Mishra and R. K. Sharma, "Dynamic power management of PV based islanded microgrid using hybrid energy storage," in *Proceedings of IEEE 6th International Conference on Power Systems (ICPS)*, New Delhi, India, Mar. 2016, pp. 1-6.

[3] C. Natesan, S. Ajithan, S. Chozhavendhan *et al*., "Power management strategies in microgrid: a survey," *International Journal of Renewable Energy Research*, vol. 5, no. 2, pp. 334-340, Jan. 2015.

[4] Z. Yi, W. Dong, and A. H. Etemadi, "A unified control and power management scheme for PV-battery-based hybrid microgrids for both grid-connected and islanded modes," *IEEE Transactions on Smart Grid*, vol. 9, no. 6, pp. 5975-5985, Nov. 2018.

[5] S. Pannala, N. Patari, A. K. Srivastave *et al*., "Effective control and management scheme for isolated and grid connected DC microgrid," *IEEE Transactions on Industry Applications*, vol. 56, no. 6, pp. 1-14, Dec. 2020.

[6] P. Singh and J. S. Lather, "Variable structure control for dynamic power-sharing and voltage regulation of DC microgrid with a hybrid energy storage system," *International Transaction Electrical Energy System*, vol. 30, no. 9, pp. 1-20, Jun. 2020.

[7] N. R. Tummuru, U. Manandhar, A. Ukil *et al*., "Control strategy for AC-DC microgrid with hybrid energy storage under different operating modes," *Electrical Power and Energy Systems*, vol. 104, pp. 807-816, Jan. 2019.

[8] J. Hu, Y. Shan, Y. Xu *et al*., "A coordinated control of hybrid AC/DC microgrids with PV-wind-battery under variable generation and load conditions," *Electrical Power and Energy Systems*, vol. 104, pp. 583-592, Jan. 2019.

[9] H. Mahmood, D. Michaelson, and J. Jiang, "A power management strategy for PV/battery hybrid systems in islanded microgrids," *IEEE Journal of Emerging and Selected Topics in Power Electronics*, vol. 2, no. 4, pp. 870-882, Jun. 2014.

[10] P. Sanjeev, N. P. Padhy, and P. Agarwal, "Peak energy management using renewable integrated DC microgrid," *IEEE Transactions on Smart Grid*, vol. 9, no. 5, pp. 4906-4917, Sept. 2018.

[11] S. Sahoo, S. Mishra, and N. P. Padhy, "A decentralized adaptive droop-based power management scheme in autonomous DC microgrid," in *Proceedings of IEEE PES Asia-Pacific Power and Energy Conference*, Xi'an, China, Dec. 2016, pp. 1018-1022.

[12] P. Singh and J. S. Lather, "Power management and control of a grid-independent DC microgrid with hybrid energy storage system," *Sustainable Energy Technologies and Assessments*, vol. 43, pp. 1-11, Feb. 2021.

[13] *IEEE Recommended Practice for Utility Interface of Photovoltaic (PV) System*, IEEE Standard 929, 2000.

[14] R. Kadri, J. P. Gaubert, G. Champenois *et al*., "Performance analysis of transformerless single switch quadratic boost converter for grid-connected photovoltaic systems," in *Proceedings of International Conference on Electrical Machines (ICEM)*, Rome, Italy, Sept. 2010, pp. 1-7.

[15] M. Hamzeh, A. Ghazanfari, Y. A. R. I. Mohamed *et al*., "Modelling and design of an oscillatory current sharing control strategy in DC microgrids," *IEEE Transactions on Industrial Electronics*, vol. 62, no. 11, pp. 6647-6657, Nov. 2015.

[16] B. Singh, D. T. Shahani, and A. K. Verma, "IRPT based control of a 50 kW grid interfaced solar photovoltaic power generating system with power quality improvement," in *Proceedings of 4th IEEE International Symposium on Power Electronics for Distributed Generation System (PEDG*), Rogers, USA, Apr. 2014, pp. 1-8.

[17] S. Golestan, M. Ramezani, J. Guerrero *et al*., "Moving average filter-based phase-locked loops: performance analysis and design guidelines," *IEEE Transactions on Power Electronics*, vol. 29, no. 6, pp. 2750-2763, Jun. 2014.

[18] N. R. Tummuru, M. K. Mishra, and S. Srinivas, "Dynamic energy management of renewable grid integrated hybrid energy storage system," *IEEE Transactions on Industrial Electronics*, vol. 62, no. 12, pp. 7728-7737, Dec. 2015.

[19] H. Wang, Z. Wu, G. Shi *et al*., "SOC balancing method for hybrid energy storage system in microgrid," in *Proceedings of 3rd IEEE International Conference on Green Energy and Applications*, Taiyuan, China, Oct. 2019, pp. 141-145.

[20] H. Bindner, T. Cronin, P. Lundsager *et al*. (2005, Jan.). Lifetime modelling of lead acid batteries. [Online]. Available: https://www.researchgate.net/publication/246687286_Lifetime_Modelling_of_Lead_Acid_Batteries

[21] *IEEE Recommended Practices and Requirements for Harmonic Control in Electrical Power Systems*, IEEE Standard 519, 1992.

[22] S. Kotra and M. K. Mishra, "A supervisory power management system for a hybrid microgrid with HESS," *IEEE Transactions on Industrial Electronics*, vol. 64, no. 5, pp. 3640-3649, May 2017.

Anindya Bharatee received the B. Tech. degree in electrical engineering from Government College of Engineering, Keonjhar, India, in 2015 and M. Tech. degree in power system engineering from Veer Surendra Sai University of Technology, Burla, India, in 2019. From 2019, she is continuing the Ph. D. degree in National Institute of Technology, Rourkela, India. Her research interests include design of power management schemes in microgrid and grid integration of renewable energy system.

Pravat Kumar Ray received the B.S. degree in electrical engineering from Indira Gandhi Institute of Technology Sarang, Odisha, India, in 2000, the M. E. degree in electrical engineering from Indian Institute of Engineering Science and Technology, Shibpur, India, in 2003, and the Ph.D. degree in electrical engineering from National Institute of Technology Rourkela, Odisha, India, in 2011. He is currently an Associate Professor with the Department of Electrical Engineering, National Institute of Technology Rourkela. He was also a Postdoctoral Fellow at Nanyang Technological University, Singapore, during January 2016 to June 2017. His research interests include signal processing and soft computing applications to power system, power quality, and grid integration of renewable energy systems.

Arnab Ghosh received the B.Tech. and M.Tech. degrees from West Bengal University of Technology, Kolkata, India, in 2010 and 2012, respectively, and the Ph. D. degree from the National Institute of Technology Durgapur, Durgapur, India, in 2017, all in electrical engineering. He is currently an Assistant Professor in the Department of Electrical Engineering, National Institute of Technology, Rourkela, India. His research interests include design of power electronics converters, renewable energy sources, microgrid and smart grid, electric vehicles, and vehicle-to-grid applications.